

Higher-order Weyl superconductors with anisotropic Weyl-point connectivity

W. B. Rui,^{1,*} Song-Bo Zhang,^{2,†} Moritz M. Hirschmann,³
Andreas P. Schnyder,³ Björn Trauzettel,² and Z. D. Wang^{1,‡}

¹*Department of Physics and HKU-UCAS Joint Institute for Theoretical and Computational Physics at Hong Kong, The University of Hong Kong, Pokfulam Road, Hong Kong, China*

²*Institute for Theoretical Physics and Astrophysics, University of Würzburg, D-97074 Würzburg, Germany*

³*Max-Planck-Institute for Solid State Research, Heisenbergstrasse 1, D-70569 Stuttgart, Germany*
(Dated: September 25, 2020)

Weyl superconductors feature Weyl points at zero energy in the three-dimensional (3D) Brillouin zone and arc states that connect the projections of these Weyl points on the surface. We report that higher-order Weyl superconductors can be realized in odd-parity topological superconductors with time-reversal symmetry being broken by periodic driving. Different from conventional Weyl points, the higher-order Weyl points in the bulk separate 2D first- and second-order topological phases, while on the surface, their projections are connected not only by conventional surface Majorana arcs, but also by hinge Majorana arcs. We show that the Weyl-point connectivity via Majorana arcs is largely enriched by the underlying higher-order topology and becomes anisotropic with respect to surface orientations. We identify the anisotropic Weyl-point connectivity as a characteristic feature of higher-order Weyl materials. As each 2D subsystem can be singled out by fixing the periodic driving, we propose how the Majorana zero modes in the 2D higher-order topological phases can be detected and manipulated in experiments.

Introduction.—The particular excitations of topological semimetals and nodal superconductors emerge around gapless degeneracies and constitute one of the main research activities in the field of topological materials [1–6]. Typical examples are Weyl and Dirac semimetals or nodal superconductors whose low-energy physics around the gapless points can be described by Weyl or Dirac Hamiltonians [7–14]. Besides exotic quasiparticles in the bulk, the bulk topology of the systems also gives rise to fascinating topological boundary states. Conventionally, in an n -dimensional topological phase, the topological boundary states are constrained to $(n - 1)$ dimensions.

Recently, inspired by higher-order topology [15–25], new topological phases, termed higher-order topological gapless phases, have attracted increasing interest [26–31]. In addition to gapless degeneracies in the n -dimensional bulk and conventional $(n - 1)$ -dimensional boundary states, these topological systems feature also $(n - d)$ -dimensional hinge or corner states with $d \geq 2$. As an important member of gapless phases, Weyl superconductors must break time-reversal or inversion symmetry [10, 11, 32, 33]. Time-reversal-symmetry breaking is particularly important, as most reported first-order (conventional) Weyl superconductors are realized in this way [34–42]. However, so far, there has been no study on higher-order Weyl superconductors (HOWSCs) with broken time-reversal symmetry. An interesting fundamental question in HOWSCs concerns their boundary states, namely, how the connectivity of surface projected Weyl points by Majorana arcs, a characteristic feature of Weyl superconductors, is reshaped by the higher-order topology.

In this Letter, we show that HOWSCs with broken

time-reversal symmetry can be realized by periodically driving a 2D second-order odd-parity topological superconductor. The periodic driving breaks time-reversal symmetry and offers an unprecedented way to extend the 2D superconductor to a third dimension with periodic boundary conditions. Weyl points can be generated in this dynamic process, which split the system into different regions of first- (FOTP) or second-order topological phases (SOTP), leading to a HOWSC. In sharp contrast to the surface Majorana arcs protected by a bulk Chern number in the FOTP regions, the hinge Majorana arcs in the SOTP regions, which are protected by inversion symmetry, depend strongly on the surface orientation due to the higher-order topology. This results in an intriguing and diverse recombination of surface and hinge Majorana arcs upon orientation change, leading to an anisotropic Weyl-point connectivity. By developing an effective boundary theory capable of describing both surface and hinge Majorana arcs, we thoroughly analyze this intricate Weyl-point connectivity of Majorana arcs in every surface orientation. Furthermore, both the FOTP and SOTP can be individually investigated as the periodic driving offers an advantage to single out each 2D slice of the system by fixing the driving parameters. We propose to control and detect the Majorana zero modes in the SOTP regions via circularly polarized light (CPL) in experiments.

Realization of HOWSCs.—Our starting point is a 2D second-order odd-parity topological superconductor that respects time-reversal symmetry. Different from previous proposals for higher-order topological superconductors [43–65], we consider an inter-orbital s -wave pairing potential with a constant magnitude Δ_0 , which may be induced

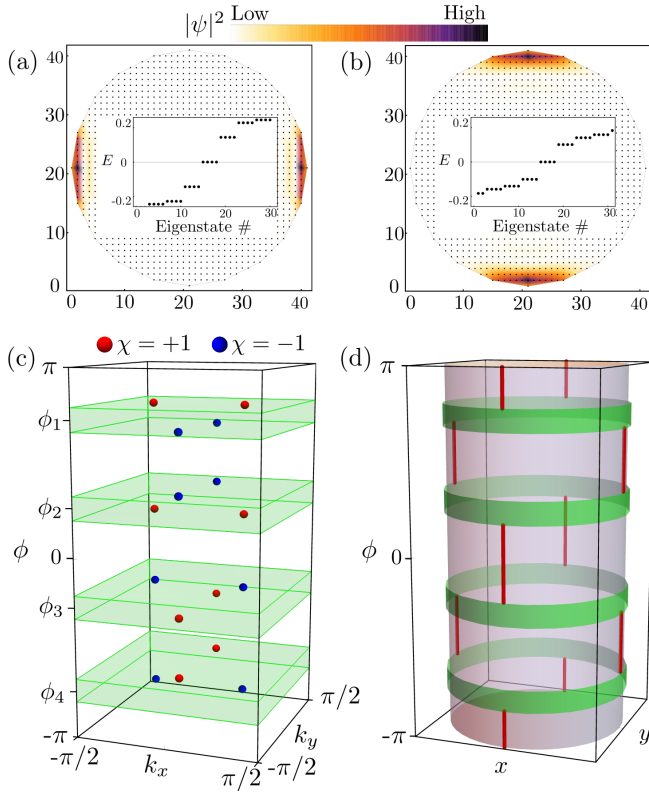


Fig. 1. (a) Two Majorana Kramers pairs (indicated by dark densities) are localized at a disk boundary in the horizontal direction; (b) Circularly polarized light with intensity $\mathcal{I} = 1.5(\omega/2m)$ and $\phi = 0$ switches the Majoranas to the vertical direction. The insets in (a) and (b) show the corresponding energy levels. (c) The 16 Weyl points of the model (2) in the synthetic 3D Brillouin zone. The red and blue points denote Weyl points with positive and negative chirality $\chi = \pm 1$, respectively. The Weyl points are grouped into four sets, denoted by their center positions ϕ_j with $j \in \{1, 2, 3, 4\}$. Each set consists of four Weyl points. Their positions divide the Brillouin zone into different topological sectors. We identify FOTPs (green area) within each of the four sets and SOTPs between neighboring sets. (d) Schematic of boundary states, obtained by stacking the 2D disks in the third dimension parameterized by ϕ . In the FOTP regions, the boundary states circle around the whole disk boundary (green belts), whereas in the SOTP regions, they form hinge states on 1D lines (red lines). The parameters are $M_0 = 3, m = 1.1, v = 1, \mu = 0, \omega = 0.1$, and $\Delta_0 = 0.6$.

via the proximity effect. The minimal Hamiltonian in momentum space can be written as $\mathcal{H} = \mathcal{H}_0 + h_\Delta$ with

$$\begin{aligned} \mathcal{H}_0 &= m(\mathbf{k})\tau_z\sigma_z + v \sin k_x s_z \sigma_x + v \sin k_y \tau_z \sigma_y - \mu\tau_z, \\ h_\Delta &= \Delta_0 \tau_y s_y \sigma_x, \end{aligned} \quad (1)$$

where $m(\mathbf{k}) = M_0 - 2m(\cos k_x + \cos k_y)$ and the Pauli matrices \mathbf{s} , $\boldsymbol{\sigma}$ and $\boldsymbol{\tau}$ act on spin, orbital, and Nambu spaces, respectively. μ is the chemical potential, M_0 , m and v are material dependent parameters. The Hamiltonian is invariant under time-reversal (\mathcal{T}) and particle-hole (\mathcal{C})

symmetry. The pairing interaction is of odd parity as indicated by $\mathcal{P}h_\Delta\mathcal{P}^{-1} = -h_\Delta$ with the inversion operator $\mathcal{P} = \sigma_z$. Correspondingly, the BdG Hamiltonian is symmetric under inversion $\tilde{\mathcal{P}}\mathcal{H}(\mathbf{k})\tilde{\mathcal{P}}^{-1} = \mathcal{H}(-\mathbf{k})$ with $\tilde{\mathcal{P}} = \tau_z\mathcal{P}$. Furthermore, spin rotation about the z axis $J_z = \tau_z s_z$ is preserved. Due to the second-order topology, our model features two 0D Majorana Kramers pairs at a disk boundary in the horizontal direction, which are protected by time-reversal and inversion symmetries [Fig. 1(a)].

Next, we show that HOWSCs can be generated on the basis of the model (1) through periodic driving. For concreteness, we consider periodic driving in the form of CPL which is shed on the system in the z direction and described by the vector potential $\mathbf{A}(t) = A_0(\cos(\omega t), \sin(\omega t + \phi), 0)$. ϕ characterizes the phase shift, A_0 the strength and ω the frequency. The CPL couples to the electrons(holes) via the Peierls substitutions $\mathbf{k} \rightarrow \mathbf{k} \pm e\mathbf{A}(t)$. To proceed analytically and elucidate our main results, we employ Floquet theory and derive a static effective Hamiltonian [66]. The effective Hamiltonian is obtained on the basis of Eq. (1) and contains a non-trivial correction that preserves spin-rotation symmetry about the z axis. We can find it as [66]

$$h(\mathbf{k}) = h_0(\mathbf{k}) + \gamma(\mathbf{k}) \cos \phi, \quad (2)$$

where $\gamma(\mathbf{k}) = (2m\mathcal{I}/\omega)(v \sin k_x \sigma_x + v \sin k_y \sigma_y - v^2 \sigma_z / 2m)$ and $h_0(\mathbf{k}) = \tau_z[(m(\mathbf{k}) + m\mathcal{I})\sigma_z + v \sin k_x \sigma_x + v \sin k_y \sigma_y - \mu] - \Delta_0 \tau_x \sigma_x$ with $\mathcal{I} = e^2 A_0^2$ corresponding to the intensity of the light. The periodic driving breaks time-reversal symmetry. Increasing \mathcal{I} above a critical value, we observe that the Majorana zero modes at the disk boundary jump from the horizontal to vertical positions [Fig. 1(b)].

The model in Eq. (2) is periodic in the parameter ϕ . We may regard it as an extra (third) dimension. Since at each ϕ time-reversal symmetry is broken, the 2D systems for fixed ϕ belong to class A and are characterized by a Chern number [67]. Strikingly, stacking these 2D systems along the ϕ direction gives a 3D Weyl superconductor with 16 Weyl points in the synthetic 3D Brillouin zone, as displayed in Fig. 1(c). These Weyl points can be grouped into four distinct sets.

In Fig. 1(d), we stack the 2D disks with different ϕ , forming a 3D cylinder. The cylinder is finite in x and y directions but periodic in ϕ direction. As can be seen by the dimensions of the boundary states, the system splits into two kinds of topological phases: (i) FOTPs within each of the Weyl-point sets, with 2D surface states at the boundary (green belts); (ii) SOTPs between different Weyl-point sets, with 1D hinge states (red lines). As the Weyl points mediate between the FOTP and SOTPs, we coin the system a HOWSC.

Anisotropic Weyl-point connectivity.—In conventional Weyl superconductors, the surface Majorana arcs that connect the projections of the Weyl points in the surface

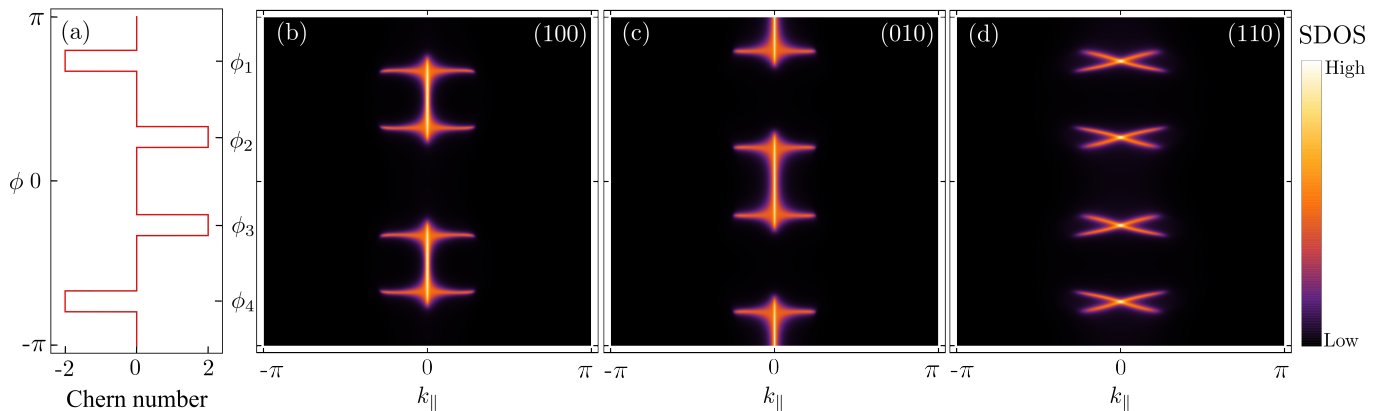


Fig. 2. Anisotropic Weyl-point connectivity due to the higher-order topology. (a) Chern number calculated within the $k_x k_y$ -planes as a function of ϕ . (b)-(d) Surface density of states on the (100), (010) and (110) surfaces, respectively. Surface Majorana arcs connect Weyl points inside each Weyl-point set and form horizontal bars. In contrast, the two hinge Majorana arcs connect Weyl points from two neighboring sets and form vertical bars, which depend strongly on the respective surface orientation. (b) On the (100) surface, the hinge Majorana arcs (vertical bars) connect the Weyl points between $\phi_1(\phi_3)$ and $\phi_2(\phi_4)$, and form two rotated “H” shapes; (c) On the (010) surface, the hinge Majorana arcs connect the Weyl points between $\phi_4(\phi_2)$ and $\phi_1(\phi_3)$; (d) On the (110) surface, the Weyl points are only connected by surface Majorana arcs in cross shapes.

Brillouin zone are protected by a non-zero Chern number. Figure 2(a) shows the Chern number calculated in $k_x k_y$ -planes for different ϕ in the HOWSC. It takes the nontrivial value of 2 or -2 inside each set of Weyl points (corresponding to the FOTP regions). In contrast, it vanishes between neighboring sets (corresponding to the SOTP regions). This can be understood from the fact that there is an equal number of Weyl points of opposite chirality in each Weyl-point set, rendering the Chern number non-zero only inside each set. Thus, the surface Majorana arcs in the FOTPs are protected by a Chern number, while the hinge Majorana arcs [68] in the SOTPs are not. In the following, we analyze the Weyl-point connectivity via these two different kinds of Majorana arcs.

To visualize the Weyl-point connectivity, we calculate the surface density of states (SDOS) for different surface orientations. Remarkably, the form of the Weyl-point connectivity is strongly anisotropic with respect to the surface orientation. Three typical cases of (100), (010), and (110) surfaces are displayed in Figs. 2(b)-(d), respectively. In Fig. 2(b), for the (100) surface, the connectivity exhibits two separated “H” shapes rotated by 90 degrees. In this case, while the surface Majorana arcs form the horizontal bars of the “H” shapes within each Weyl set, the hinge Majorana arcs form the vertical bars and connect the Weyl-point sets $\phi_1(\phi_3)$ and $\phi_2(\phi_4)$. Notably, there are double hinge Majorana arcs connecting two pairs of Weyl points with opposite chirality. Next, we turn to the (010) surface [Fig. 2(c)]. Although the connectivity still forms two rotated “H” shapes, the vertical bars composed of hinge Majorana arcs now connect different pairs of Weyl-point sets, namely $\phi_4(\phi_2)$ and $\phi_1(\phi_3)$. Finally, in Fig. 2(d) for the (110) surface,

the Weyl points can only be connected by surface Majorana arcs in cross shapes. While surface Majorana arcs can always be observed, the hinge Majorana arcs depend sensitively on surface orientation. Thus, the Weyl-point connectivity is anisotropic.

Effective boundary theory.—For a better understanding of the orientation-dependent connectivity of the Majorana arcs, it is instructive to develop a boundary theory applicable to any surface orientation. To do so, we first derive two boundary states ($\Psi_{e\uparrow}, \Psi_{h\downarrow}$) for each ϕ in the absence of pairing interactions [66]. Using these boundary states as a basis, the resulting effective boundary Hamiltonian can be obtained as

$$h_{\text{eff}}(\theta) = \begin{pmatrix} |v^+|k_{\parallel} - \mu & \tilde{\Delta}(\theta) \\ \tilde{\Delta}(\theta)^* & -|v^-|k_{\parallel} + \mu \end{pmatrix}, \quad (3)$$

where $v^{\pm} = v(1 \pm 2m\mathcal{I} \cos \phi/\omega)$, θ is the angle between the boundary and x direction, and k_{\parallel} is the momentum along the boundary (see Fig. 1 in the Supplemental Material [66]). The projected pairing potential $\tilde{\Delta}(\theta)$ is obtained as

$$\tilde{\Delta}(\theta) = \frac{i}{2} \mathcal{F} \Delta_0 \text{sgn}(v^-) (\text{sgn}(v^+ v^-) e^{i\theta} - e^{-i\theta}), \quad (4)$$

with $\text{sgn}(\cdot)$ being the sign function. The prefactor \mathcal{F} stems from the overlap of the boundary state wavefunctions [66]. It is unity for $\cos \phi = 0$ but smaller than one in general. The eigenenergies are given by $E_{\text{eff}} = (|v^+| - |v^-|)k_{\parallel}/2 + \{[(|v^+| + |v^-|)k_{\parallel}/2 - \mu]^2 + |\tilde{\Delta}(\theta)|^2\}^{1/2}$. The chemical potential μ can be absorbed in k_{\parallel} in the square root and the band gap is given by $2|\tilde{\Delta}(\theta)|$. For simplicity, we set μ to zero in the following discussion. Notably, Eq. (3) takes the form of a 1D Dirac Hamiltonian with a Dirac mass $\tilde{\Delta}(\theta)$. The mass gaps out the

boundary spectrum everywhere, except for isolated values of θ where $\tilde{\Delta}(\theta) = 0$. This is the reason why the appearance of hinge Majorana arcs depends sensitively on the surface orientation in the SOTPs.

The periodic driving preserves inversion symmetry of the system. Thus, Eq. (3) obeys $\tilde{\mathcal{P}}h_{\text{eff}}(\theta)\tilde{\mathcal{P}}^{-1} = h_{\text{eff}}(\theta + \pi)$ with $\tilde{\mathcal{P}} = \sigma_z$ the projected inversion operator, enforcing a constraint on $\tilde{\Delta}(\theta)$: $\tilde{\Delta}(\theta + \pi) = -\tilde{\Delta}(\theta)$. Obviously, $\tilde{\Delta}(\theta)$ changes sign when advancing from θ to $\theta + \pi$, leading to a gapless point along θ . The gapless point corresponds to the positions of a hinge Majorana arc. In this regard, the SOTP is protected by inversion symmetry. This result is not restricted to a specific geometry as long as inversion symmetry is preserved. From Eq. (4), we can determine the positions of the gapless points explicitly,

$$\theta = \pi[1 - \text{sgn}(v^+v^-)]/4 + n\pi, \quad n \in \{0, 1\}. \quad (5)$$

When $2m\mathcal{I}/\omega > 1$, v^+v^- changes sign at $\phi = \phi_j$ with $j \in \{1, 2, 3, 4\}$, $\phi_1 = -\phi_4 = \pi - \arccos(\omega/2m\mathcal{I})$ and $\phi_2 = -\phi_3 = \arccos(\omega/2m\mathcal{I})$. As a result, the positions in Eq. (5) switch from $\{0, \pi\}$ to $\{\pi/2, 3\pi/2\}$.

Facilitated by the boundary theory, we are now able to explain the anisotropic connectivity of the Majorana arcs obtained numerically in Fig. 2. First, for the (100) surface, $k_{\parallel} = k_y$ and $\theta = 0$. In this case, the vanishing of the mass $\tilde{\Delta}(\theta)$ in Eq. (4) is determined by $\text{sgn}(v^+v^-) = +1$, which gives $\phi \in (\phi_1, \phi_2] \cup (\phi_3, \phi_4]$. Thus, the hinge Majorana arcs connect the Weyl-point sets ϕ_1 with ϕ_2 and ϕ_3 with ϕ_4 at $k_y = 0$, as shown by the vertical bars in Fig. 2(b). Second, for the (010) surface with $k_{\parallel} = k_x$ ($\theta = \pi/2$), $\tilde{\Delta}(\theta)$ vanishes at $\text{sgn}(v^+v^-) = -1$, leading to $\phi \in (\phi_4, \phi_1] \cup (\phi_2, \phi_3]$. In this orientation, the hinge Majorana arcs instead connect ϕ_4 with ϕ_1 and ϕ_2 with ϕ_3 at $k_x = 0$, as shown by the vertical bars in Fig. 2(c). In contrast, for the (110) surface associated with $\theta = \pi/4$, $\tilde{\Delta}(\theta)$ is always non-zero for all ϕ [Fig. 2(d)]. As a result, there are no hinge arcs connecting the Weyl points.

Manipulating Majorana zero modes.—The realization of detectable and tunable Majorana zero modes is one of the main research goals in Majorana physics [69–74]. As shown in Fig. 1, by varying ϕ in the SOTPs, the positions of the Majorana zero modes at the boundary of the 2D disk are tunable. Besides this, we find that the Majorana zero modes has finite spin polarization which can also be controlled by tuning CPL.

To elucidate this manipulation, we calculate explicitly the wavefunctions of the Majorana zero modes and hence their spin polarizations. Starting with the boundary Hamiltonian Eq. (3), we first obtain the wavefunctions of the zero-energy modes. From these zero-energy modes, two Majorana zero modes can then be derived. Their wavefunctions in the Nambu and spin basis $(\Psi_{e\uparrow}, \Psi_{e\downarrow}, \Psi_{h\uparrow}, \Psi_{h\downarrow})$ can be written as $\Phi_1 \propto (e^{i\theta}\text{sgn}(v^+)\sqrt{|v^-|}, -i\sqrt{|v^+|}, e^{-i\theta}\text{sgn}(v^+)\sqrt{|v^-|}, i\sqrt{|v^+|})^T$ and $\Phi_2 \propto (-ie^{i\theta}\text{sgn}(v^+)\sqrt{|v^-|}, \sqrt{|v^+|}, ie^{-i\theta}\text{sgn}(v^+)\sqrt{|v^-|}, \sqrt{|v^+|})^T$,

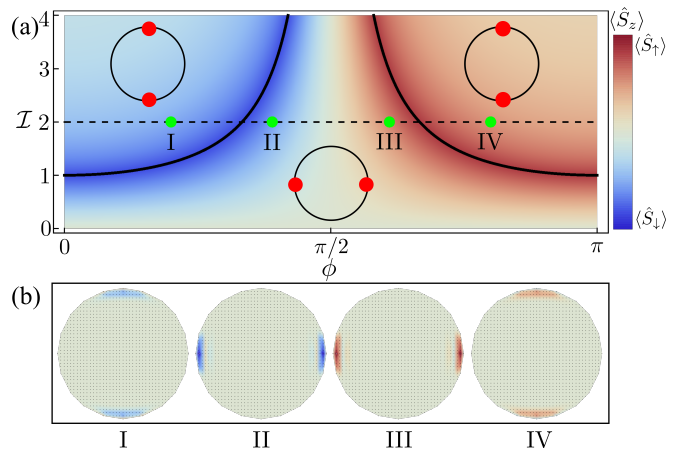


Fig. 3. Manipulation of Majorana zero modes in a 2D system. (a) The phase diagram for the second-order topological superconductor, colored by spin polarization calculated with Eq. (6). The solid lines close to the positions of Weyl points separate different SOTPs. The locations of the Majorana zero modes are sketched by the insets. The four disks in (b) show the positions and spin polarizations of the Majorana zero modes corresponding to the points at I-IV on the dashed line with $\mathcal{I} = 2$ in (a), obtained by tight-binding calculations. \mathcal{I} is given in units of $\omega/(2m)$, and all other parameter values are the same as in Fig. 1.

$\sqrt{|v^+|}^T$ [66]. The angular positions θ are either $\{0, \pi\}$ or $\{\pi/2, 3\pi/2\}$, depending on ϕ , as we have shown before. The spin polarization of the Majorana zero modes can be calculated as $\langle \hat{S}_j \rangle = \langle \Phi_j | \hat{s} | \Phi_j \rangle$, where $j \in \{1, 2\}$ and $\hat{s} = \hbar(\tau_0 + \tau_z)\mathbf{s}/2$ [75]. We find that the two Majorana zero modes have always opposite spins in x - and y -directions. Thus, they together yield vanishing $\langle \hat{S}_x \rangle = \langle \hat{S}_y \rangle = 0$ at the boundary. In contrast, for the z -component, we find an identical spin polarization for all the Majorana zero modes,

$$\langle \hat{S}_z \rangle = \frac{\hbar}{2} \frac{|v^-| - |v^+|}{|v^-| + |v^+|}, \quad (6)$$

which is independent of θ .

A phase diagram for the spin polarization of the Majorana zero modes with respect to the phase shift ϕ and intensity \mathcal{I} is plotted in Fig. 3(a). In contrast to the positions of the Majorana zero modes, the spin polarization depends continuously on the phase shift ϕ . The spin polarization splits into spin-up and spin-down regions with the border at $\phi = \pi/2$, because the correction $\gamma(\mathbf{k}) \cos \phi$ in Eq. (2) induced by the CPL vanishes and time-reversal symmetry is restored at the border. $\langle \hat{S}_z \rangle$ is an odd function of $\phi - \pi/2$. In the vicinity of $\phi = \pi/2$, it grows linearly with increasing ϕ , $\langle \hat{S}_z \rangle \approx (2\hbar m\mathcal{I}/\omega)(\phi - \pi/2)$. The spin polarization approaches its maximal value in regions where v^+ or v^- becomes zero. These regions actually separate different SOTPs, as indicated by solid lines in Fig. 3(a). Four representative cases in the diagram

marked by (I-IV) are shown in Fig. 3(b). We can see that for the phase shift ϕ at I and II, the Majorana zero modes are spin-down polarized, while at III and IV, they are spin-up polarized. We note that the spin polarization is measurable by spin-polarized scanning tunneling spectroscopy [74]. This indicates that the Majorana zero modes in our system can be manipulated and detected at the same time.

Conclusions and discussions.—We have proposed to realize time-several symmetry broken HOWSCs in second-order topological superconductors with odd-parity pairing potential by periodic driving. We have revealed an important characteristic feature of higher-order Weyl materials, namely, the anisotropic Weyl-point connectivity of the surface and hinge Majorana arcs. We have further shown the possibility to detect and manipulate the Majorana zero states by CPL.

To generate Weyl points and realize the position switching of Majorana zero modes, the frequency and intensity of CPL need to satisfy $2m\mathcal{I}/\omega > 1$. For typical values $m \simeq 50 \text{ eV}\cdot\text{\AA}^2$ (e.g., for inverted Hg(Cd)Te quantum wells [76]) and $\omega \simeq 0.1 \text{ eV}$, an experimentally feasible intensity of $eA_0 = \sqrt{\mathcal{I}} \gtrsim 0.032 \text{ \AA}^{-1}$ is sufficient for our propose. Finally, we remark that the conclusion drawn in the present work is fundamental to generic higher-order Weyl materials, including not only superconductors and semimetals, but also artificial systems. Explicitly, the model in Eq. (2) and related physics could also be simulated by superconducting quantum circuits consisting of multiple qubits [77].

This work was supported by the DFG (SPP1666 and SFB1170 “ToCoTronics”), the Würzburg-Dresden Cluster of Excellence ct.qmat, EXC2147, project-id 390858490, and the Elitenetzwerk Bayern Graduate School on “Topological Insulators”.

* wenbin.rui@gmail.com

† songbo.zhang@physik.uni-wuerzburg.de

‡ zwang@hku.hk

- [1] C.-K. Chiu, J. C. Y. Teo, A. P. Schnyder, and S. Ryu, “Classification of topological quantum matter with symmetries”, *Rev. Mod. Phys.* **88**, 035005 (2016).
- [2] G. E. Volovik, *Universe in a helium droplet* (Oxford University Press, Oxford UK, 2003).
- [3] Y. X. Zhao and Z. D. Wang, “Topological Classification and Stability of Fermi Surfaces”, *Phys. Rev. Lett.* **110**, 240404 (2013).
- [4] M. Sato and S. Fujimoto, “Majorana Fermions and Topology in Superconductors”, *Journal of the Physical Society of Japan* **85**, 072001 (2016).
- [5] M. Sato and Y. Ando, “Topological superconductors: a review”, *Reports on Progress in Physics* **80**, 076501 (2017).
- [6] N. P. Armitage, E. J. Mele, and A. Vishwanath, “Weyl and Dirac semimetals in three-dimensional solids”, *Rev. Mod. Phys.* **90**, 015001 (2018).
- [7] X. Wan, A. M. Turner, A. Vishwanath, and S. Y. Savrasov, “Topological semimetal and Fermi-arc surface states in the electronic structure of pyrochlore iridates”, *Phys. Rev. B* **83**, 205101 (2011).
- [8] S.-Y. Xu, I. Belopolski, N. Alidoust, M. Neupane, G. Bian, C. Zhang, *et al.*, “Discovery of a Weyl fermion semimetal and topological Fermi arcs”, *Science* **349**, 613 (2015).
- [9] Z. K. Liu, J. Jiang, B. Zhou, Z. J. Wang, Y. Zhang, H. M. Weng, *et al.*, “A stable three-dimensional topological Dirac semimetal Cd₃As₂”, *Nature Materials* **13**, 677 (2014).
- [10] T. Meng and L. Balents, “Weyl superconductors”, *Phys. Rev. B* **86**, 054504 (2012).
- [11] S. A. Yang, H. Pan, and F. Zhang, “Dirac and Weyl Superconductors in Three Dimensions”, *Phys. Rev. Lett.* **113**, 046401 (2014).
- [12] W. B. Rui, M. M. Hirschmann, and A. P. Schnyder, “ \mathcal{PT} -symmetric non-Hermitian Dirac semimetals”, *Phys. Rev. B* **100**, 245116 (2019).
- [13] N. Morali, R. Batabyal, P. K. Nag, E. Liu, Q. Xu, Y. Sun, B. Yan, C. Felser, N. Avraham, and H. Beidenkopf, “Fermi-arc diversity on surface terminations of the magnetic Weyl semimetal Co₃Sn₂S₂”, *Science* **365**, 1286 (2019).
- [14] D. F. Liu, A. J. Liang, E. K. Liu, Q. N. Xu, Y. W. Li, C. Chen, *et al.*, “Magnetic Weyl semimetal phase in a Kagomé crystal”, *Science* **365**, 1282 (2019).
- [15] W. A. Benalcazar, B. A. Bernevig, and T. L. Hughes, “Quantized electric multipole insulators”, *Science* **357**, 61 (2017).
- [16] Z. Song, Z. Fang, and C. Fang, “ $(d-2)$ -Dimensional Edge States of Rotation Symmetry Protected Topological States”, *Phys. Rev. Lett.* **119**, 246402 (2017).
- [17] J. Langbehn, Y. Peng, L. Trifunovic, F. von Oppen, and P. W. Brouwer, “Reflection-Symmetric Second-Order Topological Insulators and Superconductors”, *Phys. Rev. Lett.* **119**, 246401 (2017).
- [18] C. W. Peterson, T. Li, W. A. Benalcazar, T. L. Hughes, and G. Bahl, “A fractional corner anomaly reveals higher-order topology”, *Science* **368**, 1114 (2020).
- [19] F. Schindler, A. M. Cook, M. G. Vergniory, Z. Wang, S. S. P. Parkin, B. A. Bernevig, and T. Neupert, “Higher-order topological insulators”, *Sci. Adv.* **4** (2018), 10.1126/sciadv.aat0346.
- [20] F. Schindler, Z. Wang, M. G. Vergniory, A. M. Cook, A. Murani, S. Sengupta, *et al.*, “Higher-order topology in bismuth”, *Nature physics* **14**, 918 (2018).
- [21] M. Serra-Garcia, V. Peri, R. Süsstrunk, O. R. Bilal, T. Larsen, L. G. Villanueva, and S. D. Huber, “Observation of a phononic quadrupole topological insulator”, *Nature* **555**, 342 (2018).
- [22] M. Ezawa, “Higher-Order Topological Insulators and Semimetals on the Breathing Kagome and Pyrochlore Lattices”, *Phys. Rev. Lett.* **120**, 026801 (2018).
- [23] L. Trifunovic and P. W. Brouwer, “Higher-Order Bulk-Boundary Correspondence for Topological Crystalline Phases”, *Phys. Rev. X* **9**, 011012 (2019).
- [24] R. Chen, C.-Z. Chen, J.-H. Gao, B. Zhou, and D.-H. Xu, “Higher-Order Topological Insulators in Quasicrystals”, *Phys. Rev. Lett.* **124**, 036803 (2020).
- [25] E. Khalaf, “Higher-order topological insulators and superconductors protected by inversion symmetry”, *Phys.*

- Rev. B **97**, 205136 (2018).
- [26] M. Lin and T. L. Hughes, “Topological quadrupolar semimetals”, *Phys. Rev. B* **98**, 241103(R) (2018).
- [27] R.-X. Zhang, Y.-T. Hsu, and S. D. Sarma, “Higher-order topological dirac superconductors”, [arXiv:1909.07980](https://arxiv.org/abs/1909.07980).
- [28] H.-X. Wang, Z.-K. Lin, B. Jiang, G.-Y. Guo, and J.-H. Jiang, “Higher-Order Weyl Semimetals”, [arXiv:2007.05068](https://arxiv.org/abs/2007.05068).
- [29] S. A. A. Ghorashi, X. Hu, T. L. Hughes, and E. Rossi, “Second-order dirac superconductors and magnetic field induced majorana hinge modes”, *Phys. Rev. B* **100**, 020509(R) (2019).
- [30] S. A. A. Ghorashi, T. Li, and T. L. Hughes, “Higher-order Weyl Semimetals”, [arXiv:2007.02956](https://arxiv.org/abs/2007.02956).
- [31] K. Wang, J.-X. Dai, L. B. Shao, S. A. Yang, and Y. X. Zhao, “Boundary criticality of \mathcal{PT} -invariant topology and second-order nodal-line semimetals”, *Phys. Rev. Lett.* **125**, 126403 (2020).
- [32] G. Y. Cho, J. H. Bardarson, Y.-M. Lu, and J. E. Moore, “Superconductivity of doped Weyl semimetals: Finite-momentum pairing and electronic analog of the $^3\text{He-A}$ phase”, *Phys. Rev. B* **86**, 214514 (2012).
- [33] G. Bednik, A. A. Zyuzin, and A. A. Burkov, “Superconductivity in Weyl metals”, *Phys. Rev. B* **92**, 035153 (2015).
- [34] P. K. Biswas, H. Luetkens, T. Neupert, T. Stürzer, C. Baines, G. Pascua, *et al.*, “Evidence for superconductivity with broken time-reversal symmetry in locally non-centrosymmetric SrPtAs”, *Phys. Rev. B* **87**, 180503(R) (2013).
- [35] M. H. Fischer, T. Neupert, C. Platt, A. P. Schnyder, W. Hanke, J. Goryo, R. Thomale, and M. Sigrist, “Chiral d -wave superconductivity in SrPtAs”, *Phys. Rev. B* **89**, 020509(R) (2014).
- [36] P. Goswami and L. Balicas, “Topological properties of possible Weyl superconducting states of URu₂Si₂”, [arXiv:1312.3632](https://arxiv.org/abs/1312.3632).
- [37] I. M. Hayes, D. S. Wei, T. Metz, J. Zhang, Y. S. Eo, S. Ran, *et al.*, “Weyl Superconductivity in UTe₂”, [arXiv:2002.02539](https://arxiv.org/abs/2002.02539).
- [38] W. Wang, S. Kim, M. Liu, F. A. Cevallos, R. J. Cava, and N. P. Ong, “Evidence for an edge supercurrent in the weyl superconductor MoTe₂”, *Science* **368**, 534 (2020).
- [39] T. Yamashita, Y. Shimoyama, Y. Haga, T. D. Matsuda, E. Yamamoto, Y. Onuki, *et al.*, “Colossal thermomagnetic response in the exotic superconductor URu₂Si₂”, *Nature Physics* **11**, 17 (2015).
- [40] Y. Yanase and K. Shiozaki, “Möbius topological superconductivity in UPt₃”, *Phys. Rev. B* **95**, 224514 (2017).
- [41] Y. Yanase, “Nonsymmorphic Weyl superconductivity in UPt₃ based on E_{2u} representation”, *Phys. Rev. B* **94**, 174502 (2016).
- [42] N. F. Q. Yuan, W.-Y. He, and K. T. Law, “Superconductivity-induced ferromagnetism and Weyl superconductivity in Nb-doped Bi₂Se₃”, *Phys. Rev. B* **95**, 201109(R) (2017).
- [43] C.-H. Hsu, P. Stano, J. Klinovaja, and D. Loss, “Majorana Kramers Pairs in Higher-Order Topological Insulators”, *Phys. Rev. Lett.* **121**, 196801 (2018).
- [44] T. Liu, J. J. He, and F. Nori, “Majorana corner states in a two-dimensional magnetic topological insulator on a high-temperature superconductor”, *Phys. Rev. B* **98**, 245413 (2018).
- [45] Z. Yan, F. Song, and Z. Wang, “Majorana Corner Modes in a High-Temperature Platform”, *Phys. Rev. Lett.* **121**, 096803 (2018).
- [46] Q. Wang, C.-C. Liu, Y.-M. Lu, and F. Zhang, “High-Temperature Majorana Corner States”, *Phys. Rev. Lett.* **121**, 186801 (2018).
- [47] X. Zhu, “Tunable Majorana corner states in a two-dimensional second-order topological superconductor induced by magnetic fields”, *Phys. Rev. B* **97**, 205134 (2018).
- [48] X. Zhu, “Second-Order Topological Superconductors with Mixed Pairing”, *Phys. Rev. Lett.* **122**, 236401 (2019).
- [49] M. Geier, L. Trifunovic, M. Hoskam, and P. W. Brouwer, “Second-order topological insulators and superconductors with an order-two crystalline symmetry”, *Phys. Rev. B* **97**, 205135 (2018).
- [50] Z. Yan, “Higher-Order Topological Odd-Parity Superconductors”, *Phys. Rev. Lett.* **123**, 177001 (2019).
- [51] Y. Volpez, D. Loss, and J. Klinovaja, “Second-Order Topological Superconductivity in π -Junction Rashba Layers”, *Phys. Rev. Lett.* **122**, 126402 (2019).
- [52] R.-X. Zhang, W. S. Cole, and S. Das Sarma, “Helical Hinge Majorana Modes in Iron-Based Superconductors”, *Phys. Rev. Lett.* **122**, 187001 (2019).
- [53] S.-B. Zhang and B. Trauzettel, “Detection of second-order topological superconductors by Josephson junctions”, *Phys. Rev. Research* **2**, 012018 (2020).
- [54] K. Plekhanov, M. Thakurathi, D. Loss, and J. Klinovaja, “Floquet second-order topological superconductor driven via ferromagnetic resonance”, *Phys. Rev. Research* **1**, 032013 (2019).
- [55] Y.-J. Wu, J. Hou, Y.-M. Li, X.-W. Luo, X. Shi, and C. Zhang, “In-Plane Zeeman-Field-Induced Majorana Corner and Hinge Modes in an s -Wave Superconductor Heterostructure”, *Phys. Rev. Lett.* **124**, 227001 (2020).
- [56] X.-H. Pan, K.-J. Yang, L. Chen, G. Xu, C.-X. Liu, and X. Liu, “Lattice-Symmetry-Assisted Second-Order Topological Superconductors and Majorana Patterns”, *Phys. Rev. Lett.* **123**, 156801 (2019).
- [57] J. Ahn and B.-J. Yang, “Higher-order topological superconductivity of spin-polarized fermions”, *Phys. Rev. Research* **2**, 012060 (2020).
- [58] S.-B. Zhang, A. Calzona, and B. Trauzettel, “All-electrically tunable networks of Majorana bound states”, *Phys. Rev. B* **102**, 100503(R) (2020).
- [59] S.-B. Zhang, W. B. Rui, A. Calzona, S.-J. Choi, A. P. Schnyder, and B. Trauzettel, “Topological and holonomic quantum computation based on second-order topological superconductors”, [arXiv:2002.05741](https://arxiv.org/abs/2002.05741).
- [60] A. Tiwari, M.-H. Li, B. A. Bernevig, T. Neupert, and S. A. Parameswaran, “Unhinging the Surfaces of Higher-Order Topological Insulators and Superconductors”, *Phys. Rev. Lett.* **124**, 046801 (2020).
- [61] K. Laubscher, D. Loss, and J. Klinovaja, “Majorana and parafermion corner states from two coupled sheets of bilayer graphene”, *Phys. Rev. Research* **2**, 013330 (2020).
- [62] Y.-T. Hsu, W. S. Cole, R.-X. Zhang, and J. D. Sau, “Inversion-Protected Higher-Order Topological Superconductivity in Monolayer WTe₂”, *Phys. Rev. Lett.* **125**, 097001 (2020).
- [63] X. Wu, X. Liu, R. Thomale, and C.-X. Liu, “High- T_c Superconductor Fe(Se,Te) Monolayer: an Intrinsic, Scalable and Electrically-tunable Majorana Platform”, [arXiv:1905.10648](https://arxiv.org/abs/1905.10648).

- [64] Y. Peng, “Floquet higher-order topological insulators and superconductors with space-time symmetries”, *Phys. Rev. Research* **2**, 013124 (2020).
- [65] R. W. Bomantara and J. Gong, “Measurement-only quantum computation with Floquet Majorana corner modes”, *Phys. Rev. B* **101**, 085401 (2020).
- [66] See the Supplemental Material for details.
- [67] A. P. Schnyder, S. Ryu, A. Furusaki, and A. W. W. Ludwig, “Classification of topological insulators and superconductors in three spatial dimensions”, *Phys. Rev. B* **78**, 195125 (2008).
- [68] We refer to the boundary states that have the same origin like the hinge boundary states as "hinge Majorana arcs" on a 2D surface.
- [69] A. Y. Kitaev, “Unpaired Majorana fermions in quantum wires”, *Physics-Uspekhi* **44**, 131 (2001).
- [70] J. Alicea, “New directions in the pursuit of majorana fermions in solid state systems”, *Reports on Progress in Physics* **75**, 076501 (2012).
- [71] V. Mourik, K. Zuo, S. M. Frolov, S. R. Plissard, E. P. A. M. Bakkers, and L. P. Kouwenhoven, “Signatures of Majorana Fermions in Hybrid Superconductor-Semiconductor Nanowire Devices”, *Science* **336**, 1003 (2012).
- [72] R. M. Lutchyn, J. D. Sau, and S. Das Sarma, “Majorana fermions and a topological phase transition in semiconductor-superconductor heterostructures”, *Phys. Rev. Lett.* **105**, 077001 (2010).
- [73] D. Aasen, M. Hell, R. V. Mishmash, A. Higginbotham, J. Danon, M. Leijnse, *et al.*, “Milestones Toward Majorana-Based Quantum Computing”, *Phys. Rev. X* **6**, 031016 (2016).
- [74] H.-H. Sun, K.-W. Zhang, L.-H. Hu, C. Li, G.-Y. Wang, H.-Y. Ma, *et al.*, “Majorana Zero Mode Detected with Spin Selective Andreev Reflection in the Vortex of a Topological Superconductor”, *Phys. Rev. Lett.* **116**, 257003 (2016).
- [75] D. Sticlet, C. Bena, and P. Simon, “Spin and Majorana Polarization in Topological Superconducting Wires”, *Phys. Rev. Lett.* **108**, 096802 (2012).
- [76] M. König, H. Buhmann, L. W. Molenkamp, T. Hughes, C.-X. Liu, X.-L. Qi, and S.-C. Zhang, “The Quantum Spin Hall Effect: Theory and Experiment”, *Journal of the Physical Society of Japan* **77**, 031007 (2008).
- [77] X. Tan, Y. X. Zhao, Q. Liu, G. Xue, H.-F. Yu, Z. D. Wang, and Y. Yu, “Simulation and Manipulation of Tunable Weyl-Semimetal Bands Using Superconducting Quantum Circuits”, *Phys. Rev. Lett.* **122**, 010501 (2019).